Cryogenic fluid dynamics of pressure swirl injectors at supercritical conditions

Nan Zong and Vigor Yang
Department of Mechanical and Nuclear Engineering, The Pennsylvania State University, University Park, Pennsylvania 16802, USA

(Received 25 July 2007; accepted 27 November 2007; published online 27 May 2008)

A comprehensive numerical analysis has been conducted to explore the development of liquid-oxygen (LOX) flow in pressure swirl injectors operating at supercritical pressures. The model is based on full-conservation laws and accommodates real-fluid thermodynamics and transport phenomena over the entire range of fluid states of concern. Three different flow regimes with distinct characteristics, the developing, stationary, and accelerating regimes, are identified within the injector. Results are compared to predictions from classical hydrodynamics theories to acquire direct insight into the flow physics involved. In addition, various flow dynamics are investigated by means of the spectral and proper-orthogonal-decomposition techniques. The interactions between the hydrodynamic instabilities in the LOX film and acoustic oscillations in the gaseous core are clearly observed and studied. The influences of flow conditions (mass flowrate, swirl strength of the injected fluid, and ambient pressure) and injector geometry (injector length and tangential entry location) on the injector flow behavior are systematically characterized in terms of the LOX film thickness and spreading angle. The axial and azimuthal momentum exchange and loss mechanisms are also examined. © *2008 American Institute of Physics*. [DOI: 10.1063/1.2905287]

I. INTRODUCTION

This paper deals with the cryogenic fluid dynamics of a pressure swirl injector, as schematically shown by the center element of a coaxial injector in Fig. 1. The configuration is representative of contemporary liquid-propellant rocket injectors for liquid/liquid and gas/liquid mixtures.[1] Liquid propellant is tangentially introduced into the center post and then forms a swirling film attached to the wall due to centrifugal force. A hollow gas core exists in the center region in accordance with the conservation of angular momentum. The film exits the injector as a thin sheet and impinges onto the surrounding fuel stream. The swirl injection/atomization process basically involves two mechanisms: Disintegration of the liquid sheet as it swirls and stretches and sheet breakup due to the interaction with the surrounding coaxial flow. In spite of the broad applications of swirl coaxial injectors, fundamental studies on the mixing and combustion processes appear to be limited, especially at scales sufficient to identify the underlying mechanisms dictating the flow evolution and flame dynamics, and at high pressures.

Compared to jet injectors, swirl injectors in liquid-propellant rocket engines distinguish themselves in several aspects.[1] First, the nonuniform mixing of propellants in the jet core region is avoided and the intraelement mixing is significantly improved because of the outward spreading of the liquid spray.[2] High mixing efficiency is, thus, possible even for a large injector flowrate. Second, the large flow passage in a swirl injector renders the atomization characteristics to be less sensitive to manufacturing errors. The injector is also less susceptible to choking and cavitation. Third, the injected fluid is discharged into the chamber as a hollow spray cone. The thickness of the liquid film becomes thinner as it swirls and spreads outward. The resultant mean diameter of droplets is 2.2 to 2.5 times smaller than that produced by a jet injector with the same pressure drop and mass flowrate. The droplet size distribution is also more uniform. Finally, rocket swirl injectors feature large aspect ratios of up to 20, due to the manifolding considerations of propellant supply. The viscous loss along the injector wall exerts significant influence on the flow evolution and subsequently alters liquid atomization characteristics.

Hulka *et al.*[2–4] conducted a series of coldflow studies to optimize the design of swirl coaxial injectors for liquid rockets. Three different types of experiments were performed in a quiescent, atmospheric environment. Still photographs were first taken to measure the spreading angle of a water spray without a surrounding coflow. The circumferential spray uniformity and droplet size distribution were then measured under conditions with and without coflow nitrogen gas by means of a grid patternator and a Malvern droplet size analyzer, respectively. The coflow reduces the mean droplet size but widens the droplet size distribution. Measurements were also made of the Rupe mixing efficiency by using water and a sucrose solution to simulate liquid oxygen (LOX) and gaseous hydrogen, respectively. A broad range of fuel-to-oxidizer mixture (0.94–17.8) and velocity (1.15–4.28) ratios at 1 atm was considered. The mixing efficiency could be greatly enhanced by increasing the initial swirl strength of the oxidizer, which is a function of the injector geometric characteristic parameter. The oxidizer mass flowrate has little influence on the mixing efficiency. Thus, an oxidizer swirl element with a mass flowrate greater than that of a shear coaxial injector can still achieve better mixing efficiency.

A similar cold-flow experiment with water and nitrogen as injectants was performed by Sasaki *et al.*[5] at room condi-

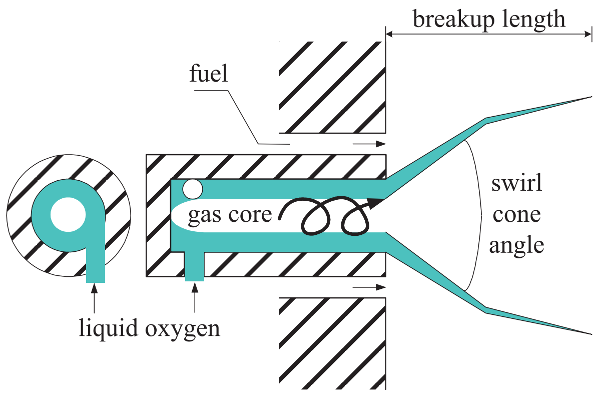

FIG. 1. (Color) Schematic of swirl coaxial injector.

tions. Special attention was given to the effect of the center post recess, which tends to narrow the spreading angle and cause a deformation of the spray cone. The influence of the annular coflow on spray characteristics was also investigated. The swirling liquid sheet that blocked the outer gas-flow passage in a recessed injector was blown off in a mushroom shape accompanied with a high-intensity screaming sound. This phenomenon, known as self-pulsation, may result in reduced combustion efficiency and high-amplitude pressure oscillations in the chamber.[1,6]

The recess effects of the center element on the mixing characteristics of a swirl coaxial injector were also examined by Han *et al.*[7] and Kim *et al.*[8] by using kerosene as the fuel and water as the oxidizer simulant. Backlight stroboscopic photographs were taken to determine the liquid spreading angle and breakup length. The median droplet size, propellant mass distribution, and mixing efficiency were measured by using a phase Doppler particle analyzer (PDPA) and a mechanical patternator. The influence of the inner-stream spreading angle was taken into account by considering four different recess numbers in the range of 0.71–1.37, defined as the ratio of the recess length to the distance from the center post to the position where the swirling liquid sheet impinges onto the outer wall of the annular passage. The mixing efficiency and propellant mass distribution were found to be very sensitive to the recess length. The Sauter mean diameter of droplets decreased slightly with increasing recess length and could be correlated with the empirical equations suggested by Lefebvre[9] and Jones.[10]

Marchione *et al.*[11] recently used a PDPA system to measure the mean droplet size and velocity profiles of a kerosene spray produced by a swirl injector. The experiment was conducted in a quiescent environment at 1 atm. Instantaneous images were taken with a high-speed charge-coupled device camera to analyze both the static and oscillatory behaviors of the spray. The spray angle estimated based on the measured mean droplet size and velocity agreed well with the results derived from the images. Two oscillation modes of the spray at a low frequency of 100 Hz and a high frequency of 1800 Hz were identified by analyzing the Mie scattering intensity in different regions. Those modes of oscillation could induce a variation of the local air/fuel ratio.

All the aforementioned studies[2–5,7,8,11] were conducted at 1 atm without considering the effects of the elevated pressures typically encountered in operational liquid-propellant rocket engines. Strakey *et al.*[12] investigated the spray characteristics of swirl coaxial injectors over a broad range of liquid-to-gas momentum ratios (0.1–100) at a chamber pressure of 2.97 MPa by using water and helium/nitrogen as propellant simulants. The spreading angle of the liquid spray decreases with the increase in the coaxial gas momentum and appears almost identical to that produced by a shear coaxial injector at the lowest liquid-to-gas momentum ratio (0.1). The mean droplet size, however, becomes smaller compared to that of a shear coaxial injector at the same flowrate. Recently, Kim *et al.* studied the effects of ambient gas density on the liquid-sheet spreading angle and breakup length of single swirl[13] and swirl coaxial[14] injectors. Water was employed as the oxidizer simulant. The measured spray angle prior to the sheet breakup remains to be almost fixed in the pressure range of 1–40 atm. The sheet breakup length, however, decreases with increasing pressure due to the enhanced aerodynamic force as the ambient gas density increases. Ela[15] conducted hot-fire experiments for multielement swirl injectors with LOX and gaseous hydrogen at mixture ratios of 5.2–6.9 and a chamber pressure of 10.3 MPa. Results indicated that the C^* efficiency increases with increasing mixture ratio. Hot-fire studies of LOX and gaseous hydrogen were also performed by Tamura and co-workers[16,5] for both single- and multielement swirl injectors at moderate chamber pressures (2.6–3.5 MPa) and mixture ratios of 4.0–8.0. It was reported that an enhanced C^* efficiency could be obtained at a greater mixture ratio.

In addition to experimental studies, numerical simulations were recently performed to explore the flow evolution of swirl coaxial injectors. Kim and Heister[17] investigated hydrodynamic instabilities of the swirling liquid jet within the recessed region of a swirl coaxial injector. A locally homogeneous flow model, previously developed for treating flow instabilities in shear coaxial injectors,[18] was adopted, by assuming the thermodynamic and momentum equilibria between the gas and liquid phases throughout the entire flowfield. The approach also employed an incompressible-flow assumption with prespecified gas and liquid densities. Real-fluid thermodynamics and property variations inherent in operational injector flows were not taken into account to simplify the analysis. Initial results indicated that the swirling motion and fluctuation of the injected liquid became more pronounced with an increase in the gas-to-liquid density ratio. Park and Heister[19] simulated the free surface and spray shape of injected liquid in a swirl injector. The analysis was based on a boundary element method along with the assumption of an axisymmetrical, inviscid, and incompressible flow. Calculated film thickness and spray cone angle agreed well with those predicted by the classical theory. Canino *et al.*[20] studied the flow development behind the center post in a swirl coaxial injector. Emphasis was placed on the vortex-shedding characteristics due to the bluff-body dynamics within the injector passage.

Although much useful information has been obtained about the liquid atomization and mixing characteristics of swirl coaxial injectors, most existing studies were conducted either at room temperatures by using water as the oxidizer simultant,[2–5,7,8,11–14] or at hot-fire conditions,[5,15,16] where the available diagnostics are limited by the difficulties in probing the flowfield in such a high-pressure, high-temperature environment. Very limited effort has been applied to investigate detailed injector flow dynamics under conditions representative of operational rocket engines, where the chamber pressure often exceeds the thermodynamic critical pressure of the injected fluid. Furthermore, the flow evolution within the injector has not been carefully explored, except for the analytic studies based on classical hydrodynamics theories discussed in Refs. 1 and 21 and numerical studies based on an incompressible-flow assumption.[17]

The purpose of the present work is to remedy these deficiencies by conducting high-fidelity simulations of cryogenic fluid dynamics of swirl injectors at supercritical pressures, mimicking the configurations and flow conditions of contemporary rocket engines by using LOX as the oxidizer.[22] The formulation accommodates full-conservation laws and takes into account real-fluid thermodynamics and transport phenomena. The specific objectives of the study are the following: (1) To characterize the detailed flow physics in the injector flow path, (2) to explore various underlying mechanisms dictating the fluid atomization and energy-transfer behaviors, and (3) to identify and prioritize key injector design attributes and operating conditions critical to the injector performance.

II. THEORETICAL FORMULATION

The basis of the present study is the general theoretical framework for treating supercritical fluid injection and mixing, as detailed by Meng *et al.*[23] and Zong *et al.*[24] The approach has been used to investigate the transport and dynamics of droplets,[23] jet mixing,[24] and chemically reacting shear flows[25] over a broad range of thermodynamic states and flow conditions. In brief, the formulation accommodates complete conservation equations of mass, momentum, energy, and species transport. Full account is taken of general fluid thermodynamics and transport phenomena over the entire temperature and pressure regimes of concern. Turbulence closure is achieved by means of a large-eddy-simulation (LES) technique, in which large-scale motions are calculated explicitly, and the effects of unresolved small-scale turbulence are either analytically or empirically modeled. The governing Favre-filtered conservation equations are derived by filtering small-scale dynamics from resolved scales over a well-defined set of spatial and temporal intervals.[26,27] The effects of subgrid-scale (SGS) motions are treated by using the approach proposed by Erlebacher *et al.*[28] which employs a Favre-averaged generalization of the Smagorinsky eddy viscosity model. The Smagorinsky coefficient C_R (≈ 0.01) and C_I (≈ 0.007) are empirically determined.[29] It should be noted that accurate modeling of SGS dynamics under supercritical conditions remains to be a challenging task, due to complications arising from rapid property variations and real-fluid thermodynamics and transport. Very limited effort has been applied so far to quantify the effects of real-fluid thermodynamics on small-scale turbulent structures, and a well-calibrated SGS model for supercritical fluid flows is currently not available. This issue will be addressed in our subsequent work.

The fluid volumetric behavior is evaluated by using a modified Soave–Redlich–Kwong equation of state[30] because of its validity over a broad range of fluid states and simplicity of numerical implementation. Thermodynamic properties, such as enthalpy, Gibbs energy, and constant-pressure specific heat, are directly derived from fundamental thermodynamic theories. They are expressed as the sum of an ideal-gas property at the same temperature and a thermodynamic departure function accounting for dense-fluid correction.[31] Transport properties, such as viscosity and thermal conductivity, are estimated by using an extended corresponding-state theory[32,33] along with a 32-term Benedict–Webb–Robin equation of state. Mass diffusivity is obtained by the Takahashi method calibrated for high-pressure conditions.[34] The implementation and validation of the property evaluation schemes are detailed in Refs. 23 and 31.

III. NUMERICAL FRAMEWORK

The theoretical formulation outlined above is numerically solved by means of a preconditioning scheme incorporating a unified treatment of general fluid thermodynamics.[35] All the numerical properties, including the preconditioning matrix, Jacobian matrices, and eigenvalues, are directly derived from fundamental thermodynamics theories, rendering a self-consistent and robust algorithm. The numerical formulation can accommodate any equation of state and is valid for fluid flows at all speeds and at all fluid thermodynamic states. Further efficiency is achieved by employing temperature instead of enthalpy as the primary dependent variable in the preconditioned energy equation.[36] This procedure eliminates laborious iterations in solving the equation of state for temperature and, consequently, facilitates the load balance among computational blocks in a distributed computing environment. The resultant scheme is highly efficient and suitable for parallel processing.

The numerical framework employs a density-based, finite-volume methodology along with a dual-time-step integration technique.[37] Temporal discretization is obtained by using a second-order backward differencing scheme, and the inner-loop pseudotime term is integrated with a four-step Runge–Kutta scheme. Spatial discretization is achieved with a fourth-order, central-difference scheme in generalized coordinates.[38] A nine-point stencil is employed to evaluate the convective flux in each spatial direction to improve the spectral resolution of small-scale turbulence structures. Fourth-order scalar dissipation with the coefficient $\varepsilon_4 = 0.001$ is applied to ensure numerical stability with minimum contamination of the solution.

The overall accuracy of the present scheme within the context of LES was carefully assessed based on the decay of the kinetic energy of isotropic turbulence. Calculations were performed for an isotropic turbulent flow in a cubic box of a nondimensional width of 2π. The experimental results of Comet-Bellot and Corrsin[39] were selected as the benchmark with an initial Taylor Reynolds number of 80 on a 32×32

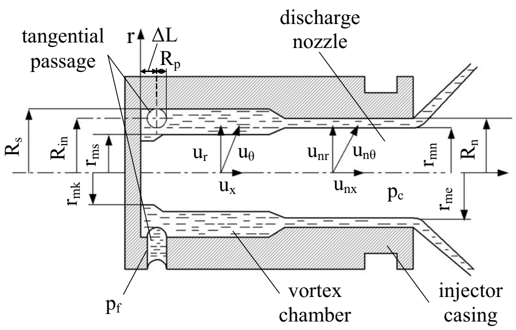

FIG. 2. Schematic of pressure swirl injector.

$\times 32$ grid. The predicted temporal evolution of turbulent kinetic energy agrees well with experimental data. The effects of numerical and SGS dissipation on the evolution of turbulent kinetic energy were further assessed by either turning those terms on or off or reducing the corresponding coefficients by one-half. Results indicated that the dissipation associated with the SGS model overshadows that of the numerical scheme, and the numerical dissipation only serves to maintain numerical stability.

The present flowfield involves exceedingly large property gradients between the injected LOX and ambient gaseous oxygen. The density ratio may reach a level of 10 for a chamber pressure 100 atm. A second-order scalar dissipation with a total-variation-diminishing switch developed by Swanson and Turkel[40] was, thus, applied to suppress numerical oscillations in regions with steep property variations. Care was also exercised to ensure sufficient grid resolution for properly capturing the hydrodynamic instability waves inherent in the LOX film.

Finally, a multiblock domain decomposition technique, along with static load balance, is employed to facilitate the implementation of parallel computation with message passing interfaces at the domain boundaries. The parallelization methodology is robust and the speedup is almost linear.

IV. INJECTOR CONFIGURATION AND BOUNDARY CONDITIONS

The dynamics of LOX injected through a pressure swirl injector into a free volume preconditioned with gaseous oxygen at a supercritical pressure is investigated. Figure 2 shows the physical model considered herein. It consists of three major parts: tangential inlets, a vortex chamber, and a discharge nozzle.[1,6] The baseline geometry and mass flowrate are summarized in Table I, where R_s, R_n, and R_p denote the radii of the vortex chamber, discharge nozzle, and tangential inlet, respectively, and L is the injector length. The parameters are chosen to be identical to those of the center element of the swirl coaxial injector in the RD-0110 liquid rocket engine, the third-stage engine for the Soyuz space launch vehicle.[41] The geometric characteristic constant, K, which determines the initial swirl strength of the injected fluid,[1] is defined as $K \equiv A_n R_{\text{in}} / A_{\text{in}} R_n$, with A_n as the discharge nozzle area, A_{in} as the total area of the tangential inlets, and R_{in} as the radial location of the tangential entry.

TABLE I. Baseline geometry and mass flowrate.

R_s (mm)	R_n (mm)	R_p (mm)	L (mm)	K	$\dot{m}$ (kg/s)
2.5	2.5	0.85	25	3.2	0.15

The computational domain includes the interior of the swirl injector and a downstream region measuring $8R_s$ and $40R_s$ in the radial and axial directions, respectively. Because of the enormous computational effort required for calculating the flow evolution in the entire regime, only a cylindrical sector with periodic boundary conditions specified in the azimuthal direction is treated. Such an axisymmetric simulation introduces several limitations: (1) the tangential inlets, which consist of six small circular ports on the injector wall, are simplified to a 1 mm wide slit on the radial boundary of the injector, (2) the flow variations in the azimuthal direction are neglected, and (3) the vortex stretching mechanism, which is responsible for the energy transfer from large- to small-scale structures in the flowfield, is not considered. In spite of those limitations, previous studies[24,42] have indicated that the present numerical analysis is able to capture many unique mechanisms dictating supercritical fluid injection and mixing dynamics, including thermodynamic nonidealities, density stratification, interfacial instability, and baroclinic vorticity production. In addition, various important unsteady flow features, such as the interactions of hydrodynamic instabilities and acoustic oscillations within the swirl injector, are well explored in the present work. The results provide a quantitative basis for identifying the key processes and injector parameters that determine the liquid-sheet breakup and atomization characteristics under supercritical pressures.

At the inlet, the bulk radial and azimuthal velocities are selected to match the mass flowrate $\dot{m}$ and the swirl strength of the injected fluid, which is estimated based on the injector geometric constant K. The fluid temperature is fixed and pressure is obtained through a one-dimensional approximation to the radial momentum equation [i.e., $\partial p / \partial r = -\rho(\partial u_r / \partial t) - u_r(\partial u_r / \partial r) + u_\theta^2 / r$]. Turbulence is provided by superimposing broadband noise onto the mean velocity profiles. The disturbances are produced by a Gaussian random-number generator with an intensity of 8% of the mean quantities, sufficient to trigger the instabilities inherent in the flowfield. A white noise with a higher turbulence intensity (10%) is also considered for the baseline case (case 1 in Table II). No obvious changes in the injector flow dynamics are observed in terms of the spectral characteristics of flow oscillations at different locations. At the downstream boundary, extrapolation of primitive variables from the interior may cause undesired reflection of numerical waves propagating into the computation domain. Thus, the characteristic boundary conditions proposed by Poinsot and Lele[43] for ideal gases and extended to real-fluid flows[36] are incorporated into the present preconditioning scheme, and a time-invariant back pressure is specified. At the radial boundary, the temperature and velocity components are extrapolated from the interior with a fixed ambient pressure. Because the computational domain is sufficiently large, the truncation effects of the radial and downstream boundaries on the injector

TABLE II. Effects of injector geometry and flow conditions on LOX film thickness and spreading angle at injector exit ($T_\infty=300$ K, and $T_{\mathrm{inj}}=120$ K).

Cases	p_∞ (atm)	L (mm)	ΔL[a] (mm)	K	$\dot{m}$ (kg/s)	Re_L (10^6)	h (mm)	2α (deg)	h_{inv} (mm)	$2\alpha_{\mathrm{inv}}$ (deg)
1	100	25	2.0	3.2	0.15	5.4	0.686	73.8	0.56	92.2
2	100	25	2.0	3.2	0.10	3.8	0.660	73.6	0.56	92.2
3	100	25	2.0	3.2	0.20	7.6	0.632	73.2	0.56	92.2
4	100	25	2.0	3.2	0.25	9.5	0.611	73.0	0.56	92.2
5	100	25	0.5	3.2	0.15	5.7	0.660	76.0	0.56	92.2
6	100	25	4.5	3.2	0.15	4.9	0.672	74.4	0.56	92.2
7	100	50	2.0	3.2	0.15	11.0	0.709	73.4	0.56	92.2
8	100	75	2.0	3.2	0.15	16.0	0.738	72.0	0.56	92.2
9	100	100	2.0	3.2	0.15	22.0	0.796	69.8	0.56	92.2
10	100	25	2.0	4.2	0.15	5.8	0.595	87.0	0.50	103.6
11	150	25	2.0	3.2	0.15	5.0	0.612	72.4	0.56	92.2
12	200	25	2.0	3.2	0.15	4.8	0.586	71.8	0.56	92.2

[a]Distance from the center of the tangential entry to the injector headend.

near-field flow dynamics are negligible. Finally, the nonslip adiabatic conditions are enforced along the solid wall.

V. RESULTS AND DISCUSSION

The liquid-film thickness h and spreading angle 2α at the injector exit are often employed to characterize the performance of a swirl injector.[1] The former dictates the size of the fluid parcel after the film breaks up, and the latter affects the intraelement mixing efficiency. The spreading angle is defined as twice the apex angle of the asymptotic cone to the hyperboloid of revolution corresponding to the profile of the spray and can be calculated by the ratio of the circumferential to the axial velocities at the injector exit, i.e., $\alpha \equiv \tan^{-1}(u_{e\theta}/u_{ex})$.[1] The key variables influencing the injector flow dynamics include the geometric constant K, injector length L, injector exit diameter D_n, and thermophysical properties of the injected fluid, such as the density ρ and viscosity μ. According to the Buckingham Pi theorem,[44] two dimensionless equations for the film thickness and spreading angle at the injector exit can be obtained in terms of those variables,

$$h/D_n = f(\rho_{\mathrm{inj}}/\rho_\infty, \mu_{\mathrm{inj}}/\mu_\infty, \mathrm{Re}_L, K), \quad (1)$$

$$\alpha = \tan^{-1} u_{e\theta}/u_{ex} = f(\rho_{\mathrm{inj}}/\rho_\infty, \mu_{\mathrm{inj}}/\mu_\infty, \mathrm{Re}_L, K), \quad (2)$$

where the subscripts inj and ∞ denote the injected fluid and ambient conditions, respectively. The Reynolds number of the liquid film is defined as $\mathrm{Re}_L = \rho_{\mathrm{inj}} u_n L/\mu_{\mathrm{inj}}$. Among those parameters, the density and viscosity ratios are fixed for a given flow condition. The geometric constant and injector length are determined by the injector configuration.

A parametric study is conducted to investigate the effects of injector geometry and operating condition on the liquid spray behavior over a pressure range of 100–200 atm. The LOX injection and ambient temperatures are fixed at 120 and 300 K, respectively. For reference, the critical pressure and temperature of oxygen are 50.4 atm and 154.6 K, respectively. Table II summarizes the injector configurations and flow parameters obtained from the present analysis. Also included for comparison are those predicted by classical swirl-injector theories for inviscid, incompressible flows (denoted by the subscript inv),[1] written in the following form:

$$h_{\mathrm{inv}} = R_n(1 - \sqrt{1-\varphi}), \quad (3)$$

$$\alpha_{\mathrm{inv}} = u_{e\theta}/u_{ex} = \tan^{-1} \sqrt{2(1-\varphi)^2/[2-\varphi-2(1-\varphi)^2]}, \quad (4)$$

where the coefficient of passage fullness φ is defined as the fractional area filled by the injected fluid in the discharge nozzle,

$$\varphi = \frac{\pi(R_n^2 - r_{mn}^2)}{\pi R_n^2} = 1 - \frac{r_{mn}^2}{R_n^2}. \quad (5)$$

As will be further elaborated, both the liquid-film thickness and spreading angle are sole functions of the injector geometric constant K and independent of such operating parameters as mass flowrate, in accordance with classical hydrodynamics theories. The situation becomes substantially different in reality due to the existence of viscous loss and property variations. Since no distinct interface exists between the injected fluid and gaseous core in a supercritical flow environment, to facilitate analysis, the numerically calculated LOX film boundary is defined as the radial position above which the mass flowrate equals the specified value at the inlet. This definition takes into account rapid fluid property variations and provides a quantitative basis for evaluating the liquid-sheet formation and breakup processes. Because the detailed velocity information can be easily retrieved from the present analysis, the film spreading angle α is evaluated based on its definition, as the inverse tangent of the ratio of the averaged azimuthal to axial velocity at the injector exit.

A typical simulation employs a 50×100 grid for the injector interior and a 150×200 grid for the downstream exterior region. The grids are clustered near the wall and the injector exit to resolve steep gradients in these regions. The smallest grid size in the radial direction is 20 μm, which falls in the inertial subrange of the turbulent kinetic energy spectrum estimated by using the Kolmogorov–Obukhow

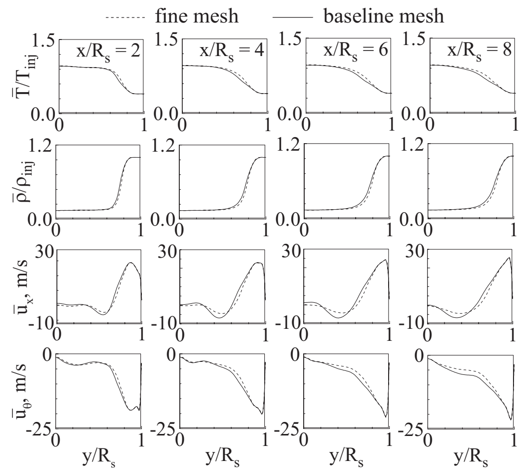

FIG. 3. Effect of grid resolution on radial distributions of mean temperature, density, and axial and radial velocity components at different axial locations (case 1: $p_\infty=10$ MPa, $T_{inj}=120$ K, $T_\infty=300$ K, $\dot{m}=0.15$ kg/s, $\Delta L=2.0$ mm).

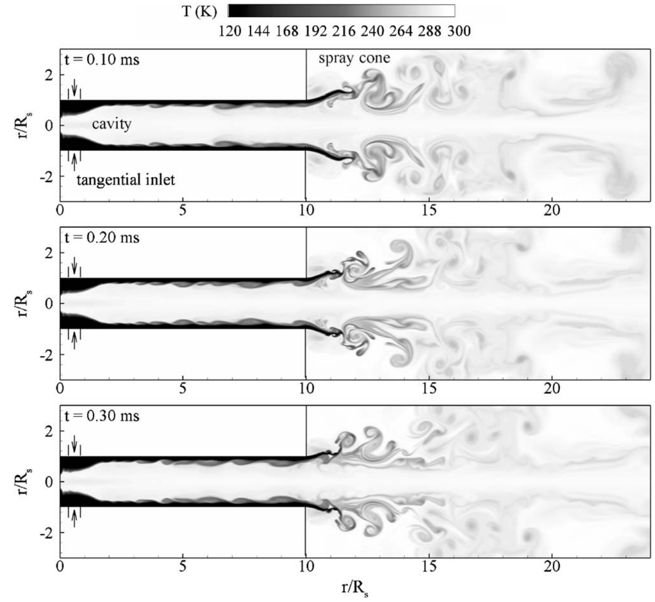

FIG. 4. Temporal evolution of temperature field (case 1: $p_\infty=10$ MPa, $T_{inj}=120$ K, $T_\infty=300$ K, $\dot{m}=0.15$ kg/s, $K=3.2$, $\Delta L=2.0$ mm).

theory. The computational domain is divided into 15 blocks, with each calculated on a single processor of a distributed-memory parallel computer. The physical time step is 1×10^{-2} ms and the maximum Courant–Friedrichs–Lewy number for the inner-loop pseudotime integration is 0.7. Each simulation is conducted for ten flow-through times for the entire domain (i.e., 0.1 s) to obtain statistically meaningful data.

A grid-independence study was performed for case 1 as part of the validation procedure. The same numerical code, injector configuration, and flow conditions are considered by using a fine mesh with a 75×160 grid for the injector interior and a 225×320 grid for the downstream exterior region. The mean grid resolution inside the injector is enhanced by 50% in each spatial direction. Figure 3 shows the radial distributions of the time-mean temperature, density, and axial and radial velocity components at different axial locations. Results for the two different grid systems are in close agreement. The maximum derivation in the entire domain is less than 5%. The effect of grid resolution on the dynamical behavior of the injector flow was also examined. The maximum relative error is 3% for both the length and speed of the hydrodynamic instability wave within the liquid film. The differences of the frequency and magnitude of the dominant pressure oscillations induced by flow instabilities are less than 5%. The results indicate that the injector dynamics have been well captured and the grid system employed is appropriate in the present work.

A. Injector flow dynamics

Figure 4 shows the temporal evolution of the temperature field for case 1 (the baseline case). LOX is tangentially introduced into the injector. The swirl-induced centrifugal force prevents the injected fluid from penetrating into the center and, consequently, gives rise to the formation of a gaseous core (referred to as cavity). A thin liquid film forms, convects downstream along the wall according to the conservation of mass and momentum, and exits from the injector as a nearly conical sheet. Several different types of flow oscillations are observed. The LOX film is intrinsically unstable and features three-dimensional hydrodynamic instability waves in both the longitudinal and circumferential directions.[45] The circumferential mode, however, cannot be observed in the present axisymmetric simulation. The longitudinal instability wave propagates within the film in a form similar to the shallow-water wave for an incompressible flow and induces oscillations of the circumferential velocity in both the axial and radial directions, which are then convected downstream with the mean flow. As the liquid film is discharged from the injector to the chamber, the Kelvin–Helmholtz type of instability emerges in the LOX sheet and, subsequently, leads to sheet breakup and droplet formation. In addition, the injector is acoustically connected with the downstream chamber. Any acoustic oscillation in the chamber may propagate upstream into the injector and affect the LOX film behavior by influencing the mass flowrate of the injected fluid.[1,6] Furthermore, strong acoustic resonance occurs if the natural frequencies of the injector and chamber match each other.[46]

Figure 5 shows a close-up view of the temperature evolution near the LOX film for the baseline case, indicating the presence of the longitudinal mode of the hydrodynamic instability. The wave grows and develops to large-scale billows as it convects downstream. The calculated wave speed is approximately 10 m/s in the region of $2\leqslant x/R_s\leqslant 9$, where the LOX film is well developed and its time-mean thickness slowly varies. A wave equation characterizing the hydrodynamic instability of a swirling liquid film can be established based on linearized conservation laws. For an inviscid, incompressible flow, with the neglect of the radial velocity and the assumption of an infinitesimal film thickness compared to the wavelength, the wave equation becomes[6]

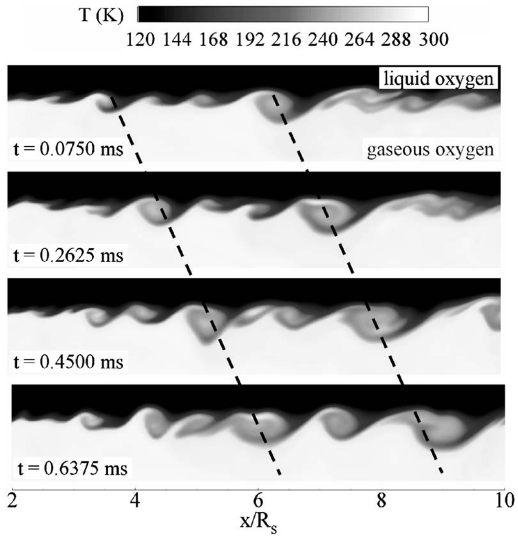

FIG. 5. Close-up view of temporal evolution of temperature field near liquid-oxygen film (case 1: $p_\infty=10$ MPa, $T_{\mathrm{inj}}=120$ K, $T_\infty=300$ K, $\dot{m}=0.15$ kg/s, $K=3.2$, $\Delta L=2.0$ mm).

$$\frac{\partial^2\xi}{\partial t^2}=\frac{1}{r_m^4}u_{\mathrm{in}}^2R_{\mathrm{in}}^2\left(\frac{R_s^2-r_m^2}{2}\right)\frac{\partial^2\xi}{\partial x^2}, \tag{6}$$

where ξ is the instantaneous displacement of the film surface, r_m is the radial distance between the injector centerline and the time-mean film surface, and u_{in} is the injection velocity at the tangential inlet. The form of the wave speed bears a close resemblance to that for shallow-water wave propagation,[6]

$$a=\sqrt{\left(\frac{u_{\mathrm{in}}^2R_{\mathrm{in}}^2}{r_m^3}\right)\left(\frac{R_s^2-r_m^2}{2r_m}\right)}. \tag{7}$$

The first parenthesized term in the square root represents the centrifugal force and the second term represents the effective thickness of the liquid film. Equation (7) results in a wave speed of 6.6 m/s based on the values of u_{in} and r_m (11 m/s and 1.9 mm, respectively). The classical hydrodynamics theory underpredicts the wave speed due to the neglect of fluid compressibility and viscous effects.

The frequency spectra of pressure fluctuations provide a more quantitative insight into the various types of instability waves involved. Figure 6 presents the results obtained at eight different positions within the injector. A small peak at 14 kHz is observed at probes 1–4, resulting from the recirculating LOX flow between the tangential inlet and the injector headend. This high-frequency oscillation is confined within the upstream region. It rapidly decays and disappears as the LOX film moves downstream due to viscous dissipation. Two dominant modes at the frequencies of 0.55 and 3.15 kHz are observed at all the probe locations. The former is closely related to the longitudinal wave of hydrodynamic instability within the LOX film. In the present case, the wave propagation speed is about 10 m/s, and the time for a disturbance to travel through the LOX film within the injector (i.e., from the tangential entry to the injector exit) is on the order of 2 ms. This leads to a characteristic frequency of 500 Hz for the longitudinal hydrodynamic instability. The result shows good agreement with the calculated frequency

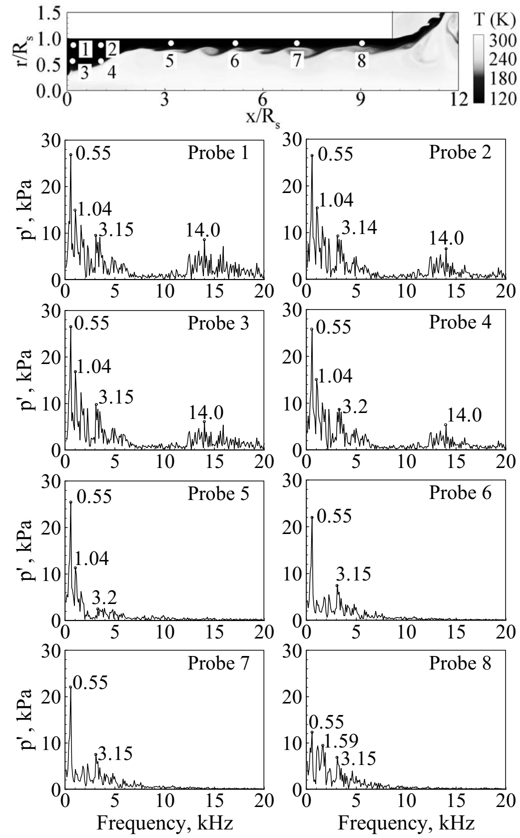

FIG. 6. Power spectral densities of pressure fluctuations at eight different locations inside injector (case 1: $p_\infty=10$ MPa, $T_{\mathrm{inj}}=120$ K, $T_\infty=300$ K, $\dot{m}=0.15$ kg/s, $K=3.2$, $\Delta L=2.0$ mm).

of 550 Hz. Figure 7 presents the frequency contents of the pressure and velocity fluctuations at probe 6. Both the axial and azimuthal velocities closely correlate with the pressure signal. As the wave propagates downstream, the local axial velocity and pressure also fluctuate to satisfy the conservation of the mass and momentum. The ensuing variation of the film thickness then causes the azimuthal velocity to oscillate in accordance with the conservation of mass and angular momentum. The lack of noticeable oscillations of the radial velocity in the low-frequency range may be attributed to the small thickness of the LOX film.

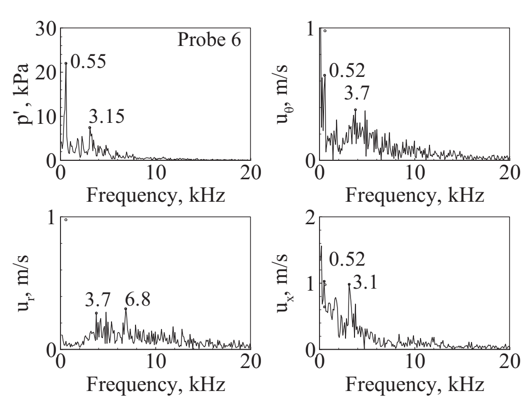

FIG. 7. Power spectral densities of pressure and velocity fluctuations at probe 6 (case 1: $p_\infty=10$ MPa, $T_{\mathrm{inj}}=120$ K, $T_\infty=300$ K, $\dot{m}=0.15$ kg/s, $K=3.2$, $\Delta L=2.0$ mm).

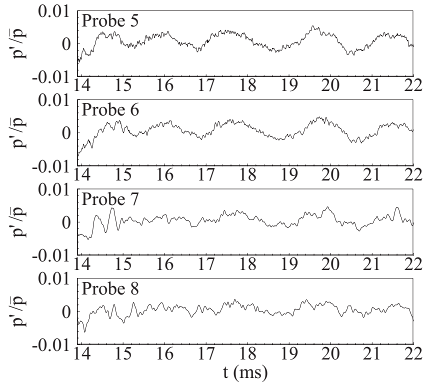

FIG. 8. Time histories of pressure oscillations at four different locations along the liquid-oxygen film (case 1: $p_\infty=10$ MPa, $T_{\mathrm{inj}}=120$ K, $T_\infty=300$ K, $\dot{m}=0.15$ kg/s, $K=3.2$, $\Delta L=2.0$ mm).

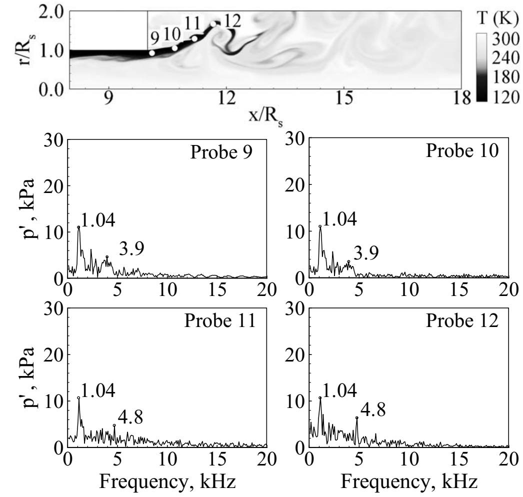

FIG. 9. Power spectral densities of pressure fluctuations at four different locations in near field of injector (case 1: $p_\infty=10$ MPa, $T_{\mathrm{inj}}=120$ K, $T_\infty=300$ K, $\dot{m}=0.15$ kg/s, $K=3.2$, $\Delta L=2.0$ mm).

The harmonic of 3.15 kHz shown in the frequency spectral of Fig. 6 may arise from the acoustic oscillation in the injector. The injector configuration considered in the present study can be acoustically treated as a quarter-wave resonator having a natural frequency

$$f = c/4(L+\Delta l), \tag{8}$$

where c is the speed of sound in the gaseous oxygen core and L is the injector length. A correction factor Δl, which is usually taken as $0.6R_n$, is employed to account for the effect of gaseous oxygen immediately downstream of the injector exit on the acoustic resonance of the injector. Under the present flow conditions of $c=340$ m/s, $L=25$ mm, and $\Delta l=1.5$ mm, the resonance frequency becomes 3.2 kHz, almost identical to the observed harmonic in Fig. 6. Figure 8 shows the time histories of pressure oscillations at probes 5–8. The low-frequency (0.55 kHz) hydrodynamic wave considerably decays in the downstream region, while the acoustic-driven, high-frequency (3.15 kHz) instability retains its magnitude in the entire LOX film.

Figure 9 shows the spectral contents of flow oscillations in the near field of the injector. A dominant frequency of 1.04 kHz is observed at all probes. This phenomenon can be attributed to the precession of the vortex core in the central toroidal recirculation zone immediately downstream of the injector exit.[47] The resultant oscillation then excites flow instabilities inside the injector, as evidenced in the frequency spectra given in Fig. 6. The LOX sheet, once it exits from the injector, is subject to the Kelvin–Helmholtz type of instability. A peak at around 3.9 kHz (probes 9 and 10) exists along the LOX sheet, which subsequently develops to 4.8 kHz (probes 11 and 12) as the liquid travels downstream. The vortex-shedding frequency can be roughly estimated by using the following empirical correlation:[48]

$$f_n = \mathrm{St}\bar{U}/\theta, \tag{9}$$

where the Strouhal number St ranges from 0.044 to 0.048 for turbulent flows. In the present study, the mean velocity $\bar{U}$ is around 10 m/s and the momentum thickness of the conic sheet is around 0.08 mm. The most unstable frequency f_n is predicted to be 5.75 kHz, which is comparable with the calculated frequency.

The injector flow dynamics are further explored by using the proper-orthogonal-decomposition (POD) technique, which extracts energetic coherent structures from the calculated flowfields. For a given flow property $f(\boldsymbol{r},t)$, the POD analysis can determine a set of orthogonal functions φ_j, $j=1,2,\ldots$, such that the projection of f onto the first n functions,

$$\hat{f}(\boldsymbol{r},t) = \bar{f}(\boldsymbol{r}) + \sum_{j=1}^{n} a_j(t)\varphi_j(\boldsymbol{r}), \tag{10}$$

has the smallest error, defined as $E(\|f-\hat{f}\|^2)$. Here, $a_j(t)$ represents the temporal variation of the jth mode, and $E(\cdot)$ and $\|\cdot\|$ denote the time average and norm in the L^2 space, respectively. The function f can be extended to a vector by introducing an appropriate inner product on $\vec{F}$. A more complete discussion of this subject can be found in Refs. 49 and 50.

The method of snapshots is implemented to compute the POD modes. The database for the POD analysis contains a total of 320 snapshots of the flowfield within the injector.

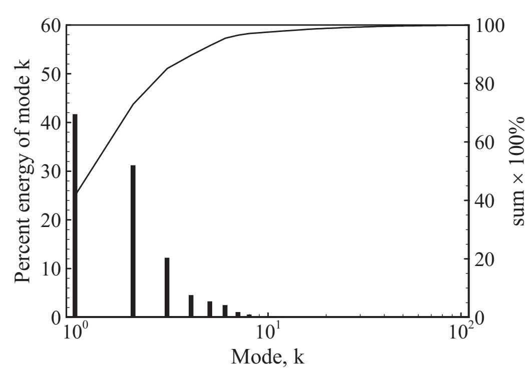

FIG. 10. Energy distribution of POD modes of pressure oscillations within injector (case 1: $p_\infty=10$ MPa, $T_{\mathrm{inj}}=120$ K, $T_\infty=300$ K, $\dot{m}=0.15$ kg/s, $K=3.2$, $\Delta L=2.0$ mm).

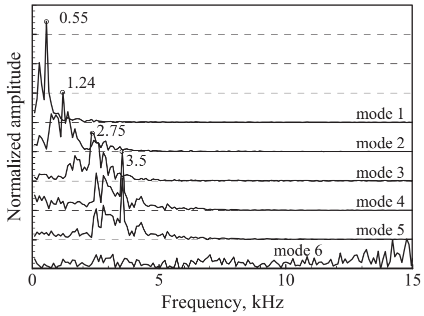

FIG. 11. Frequency spectra of time-varying coefficients of first six POD modes of pressure oscillations (case 1: $p_\infty=10$ MPa, $T_{\text{inj}}=120$ K, $T_\infty=300$ K, $\dot{m}=0.15$ kg/s, $K=3.2$, $\Delta L=2.0$ mm).

The time interval between snapshots is 50 μs, compared to the time step of 5 μs employed in the numerical simulations.

Figure 10 presents the energy distribution of the POD modes for the oscillatory pressure field of the baseline case. Here, the energy of the jth mode E_j is defined as

$$E_j = E(\|a_j(t)\varphi_j(\boldsymbol{r})\|^2). \tag{11}$$

The first six POD modes capture more than 95% of the total energy of the oscillatory flowfield. The frequency spectra of the time-varying coefficients $a_j(t)$ of these modes are shown in Fig. 11. A dominant frequency of 0.55 kHz is observed for the first mode, which is close to the characteristic frequency of the longitudinal hydrodynamic instability wave in the LOX film. The second and third modes are associated with the oscillations resulting from the precession of the toroidal recirculating flow downstream of the injector exit. The fourth and fifth modes have the identical frequency of 3.5 kHz, corresponding to the natural acoustic oscillations within the injector. It should be noted that the frequency contents of the POD modes slightly deviate from those presented in Fig. 6 (i.e., pressure oscillations in the LOX film). The POD analysis is concerned with the entire field and, consequently, provides results in a volume-average sense, as opposed to results at selected points (Fig. 6). The discrepancy becomes more noticeable in the present study, in which the flowfield is highly nonhomogeneous with a steep density stratification across the LOX film surface. Another factor contributing to the difference between Figs. 6 and 11 is the limited temporal resolution of the POD analysis, especially for the high-frequency modes.

Figure 12 shows the spatial distributions (i.e., mode shapes) of the first six modes of the oscillatory pressure field in the injector. The first mode shape is nearly one dimensional and exhibits a decaying distribution with a maximum at the head and a diminished value at the exit. The results corroborate the intimate relationship between the hydrodynamic instability wave in the LOX film and the unsteady field in the gaseous core. Any hydrodynamic disturbance in the liquid film may cause variations of the film thickness, which, in turn, produce pressure fluctuations in the free volume of the injector, mainly due to the volume dilation across the film surface induced by the local temperature changes

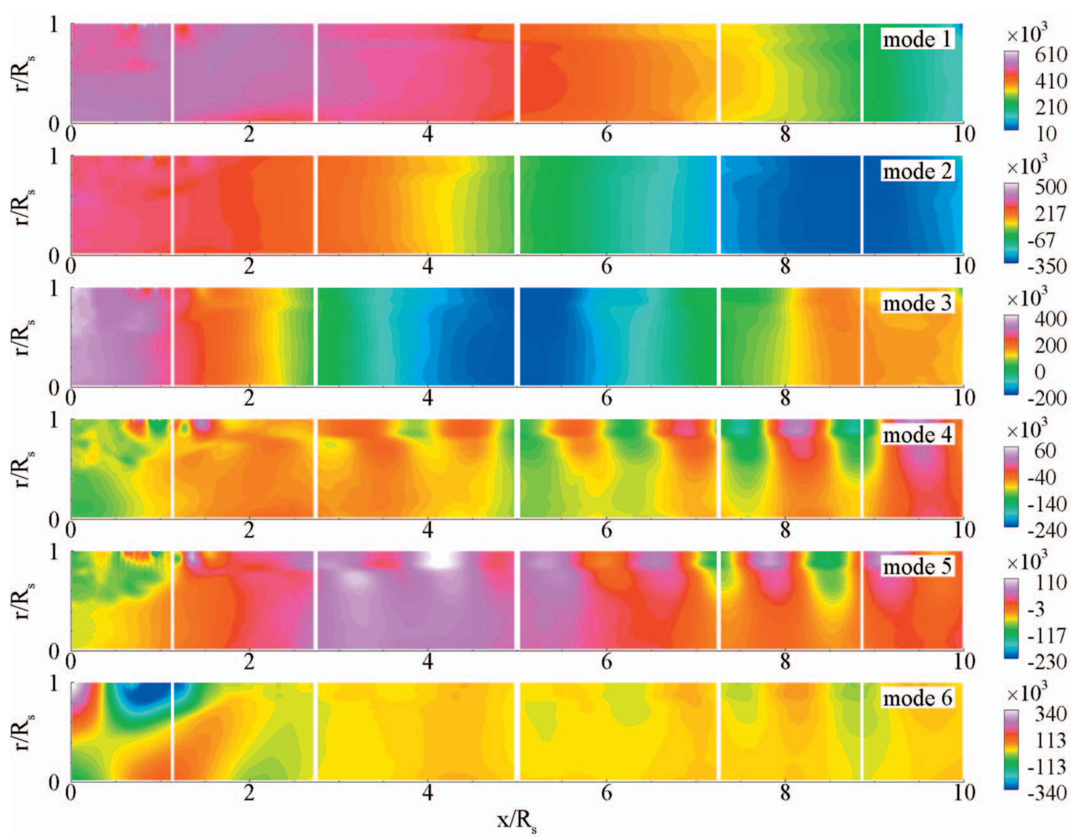

FIG. 12. (Color) Spatial distributions of first six POD modes of oscillatory pressure field within injector (case 1: $p_\infty=10$ MPa, $T_{\text{inj}}=120$ K, $T_\infty=300$ K, $\dot{m}=0.15$ kg/s, $K=3.2$, $\Delta L=2.0$ mm).

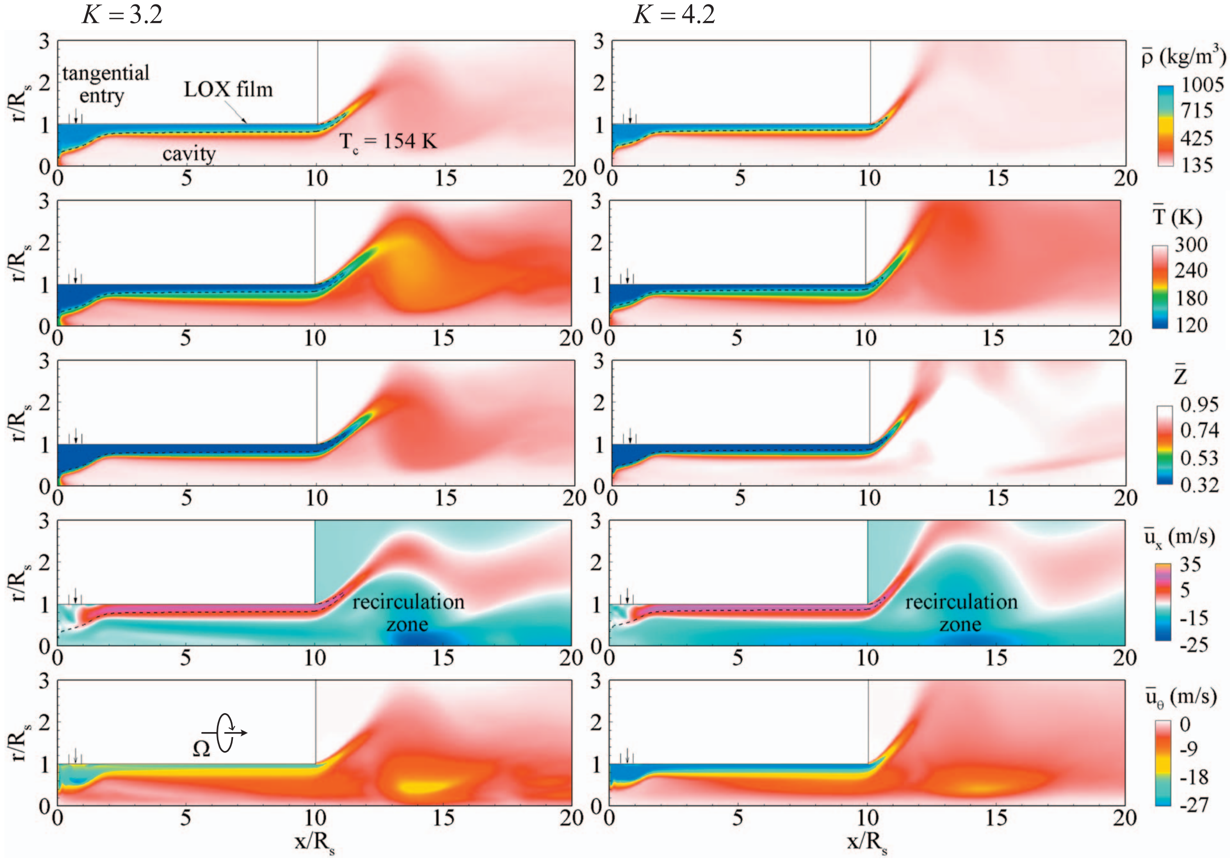

FIG. 13. (Color) Time-mean fields of density, temperature, compressibility factor, and velocity components ($p_\infty = 10$ MPa, $T_{inj} = 120$ K, $T_\infty = 300$ K, $\dot{m} = 0.15$ kg/s, $\Delta L = 2.0$ mm).

(see Fig. 5). The second and third modes are attributed to the excitation by the precession vortex core in the near field of the injector exit. The fourth and fifth modes bear quite similar structures but with a phase difference of $\pi/2$ in both time and space. This suggests the existence of a standing wave in the injector. The sixth mode reveals a dipolelike structure surrounding the tangential entry near the injector headend. The associated high-frequency oscillation is basically confined in the upstream region and rapidly decays as the fluctuation propagates downstream.

B. Mean flow properties

Figure 13 shows the time-mean fields of the density, temperature, compressibility factor, and velocities for cases 1 and 10. The corresponding geometric parameters K are 3.2 and 4.2, respectively. The critical isothermal surface of oxygen at $T_c = 154$ K, as denoted by the dashed line, is also presented to provide a reference for the LOX film boundary. The dense-fluid film near the wall and gaseous core in the cavity are clearly observed. The LOX sheet promptly mixes with the warm gas soon after exiting from the injector, instead of deeply penetrating into the chamber. Rapid volume dilation and property variations take place when the LOX mixes with the surrounding gaseous oxygen, and the local temperature transits across the inflection point on the isobaric line in the thermodynamic ρ-T diagram. Figure 14 shows the radial distributions of the time-mean flow properties at various axial locations for case 1. The velocity field indicates the presence of a swirling gaseous flow downstream of the injector exit, where the adverse pressure gradient in the axial direction produces a recirculation zone. Owing to the relatively low pressure in this region, the LOX sheet, which initially expands outward in the radial direction, converges toward the centerline, until the radial pressure gradient is balanced by the centrifugal force. As the swirl strength increases with K varying from 3.2 to 4.2, the film thickness decreases, but the spreading angle becomes wider. The recirculation zone downstream of the exit is enlarged and even extended into the injector. A similar situation was observed by Panda and McLaughlin[51] in their experimental study on swirling-jet instabilities at a swirl number of 0.5 and a Reynolds number of 57 000.

Figure 15 shows the distribution of the LOX film thickness along the injector wall for case 1, defined based on the injected mass flowrate of 0.15 kg/s and local fluid density and axial velocity. Three different flow regimes exist within the injector. In the developing region $(0 \leqslant x/R_s \leqslant 2)$ close to the injector headend, the injected LOX initially occupies a substantial fraction of the free volume, due to the small axial velocity. The fluid then converges toward the wall and forms a thin film. Downstream of the tangential inlet at $2 \leqslant x/R_s \leqslant 9$, a stationary regime emerges, in which the radial distributions of the flow properties slowly vary along the axial direction. The film thickness gradually increases due to the

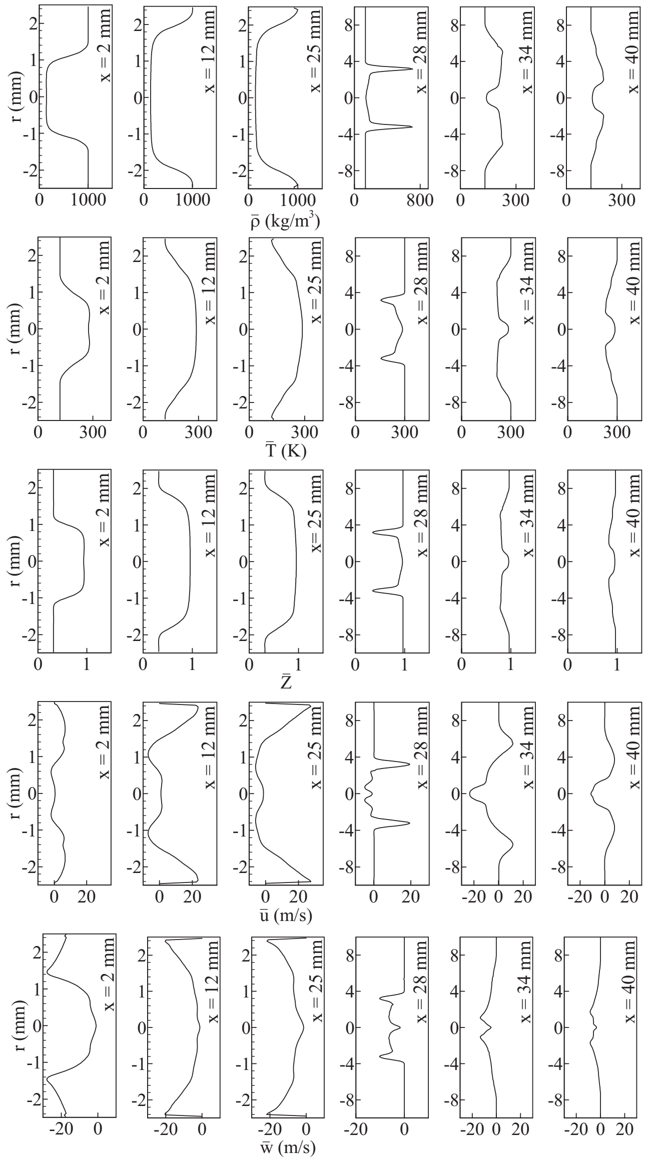

FIG. 14. Radial distributions of mean velocity components, temperature, density, and compressibility-factor at various axial locations (case 1: $p_\infty = 10$ MPa, $T_{\mathrm{inj}} = 120$ K, $T_\infty = 300$ K, $\dot{m} = 0.15$ kg/s, $K = 3.2$, $\Delta L = 2.0$ mm).

decreased axial velocity caused by viscous friction and reduced fluid density resulting from local heat transfer. Finally, as the static pressure induced by the swirling motion is converted into axial momentum close to the injector exit, the axial velocity increases and the film thickness decreases in

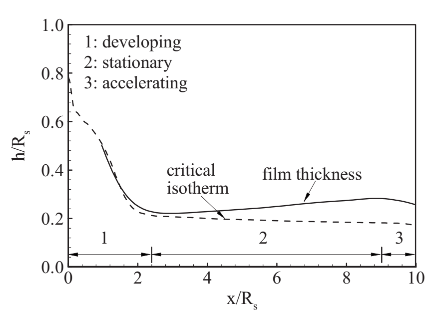

FIG. 15. Liquid-oxygen film thickness along injector wall (case 1: $p_\infty = 10$ MPa, $T_{\mathrm{inj}} = 120$ K, $T_\infty = 300$ K, $\dot{m} = 0.15$ kg/s, $K = 3.2$).

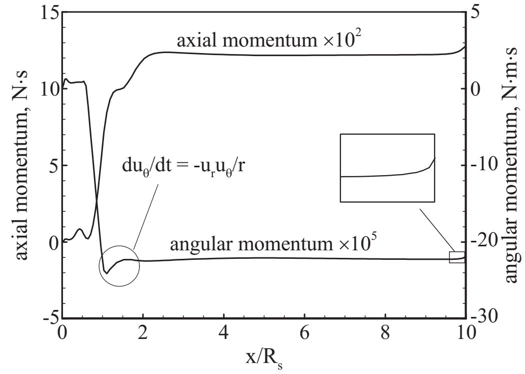

FIG. 16. Axial distributions of time-mean axial and angular momenta (case 1: $p_\infty = 10$ MPa, $T_{\mathrm{inj}} = 120$ K, $T_\infty = 300$ K, $\dot{m} = 0.15$ kg/s, $K = 3.2$).

the acceleration region ($9 \le x/R_s \le 10$). Also included in the figure is the critical isotherm of oxygen. The heat transfer from the warm ambient gas to the LOX film causes the critical isothermal surface to regress toward the injector wall.

Figure 16 shows the axial distributions of the time-averaged axial and angular momenta of the LOX film. The flow motions in both the axial and azimuthal directions are weak close to the headend. The angular momentum then rapidly increases and reaches its maximum at the trailing edge of the tangential inlet. The injected LOX is driven toward the wall by the centrifugal force and accelerates downstream according to the conservation of mass. As a consequence, the axial momentum of the LOX film rapidly increases. The transport of azimuthal momentum is more complicated and can be described by the following equation:

$$\frac{du_\theta}{dt} = -\frac{1}{\rho}\frac{\partial p}{\partial \theta} + \nu\left(\nabla^2 u_\theta + \frac{2}{r^2}\frac{\partial u_r}{\partial \theta} - \frac{u_\theta}{r^2}\right) - \frac{u_r u_\theta}{r}. \tag{12}$$

The first term on the right-hand side of Eq. (12) represents the pressure gradient in the azimuthal direction, which vanishes in the present axisymmetrical simulation. The second term denotes viscous dissipation. The third term accounts for the transfer between the radial and azimuthal momenta. This quantity vanishes in the stationary region, in which u_r is practically zero in the LOX film. The small variations of the angular momentum downstream of the tangential entry and near the injector exit (the accelerating region) arise from the rapid change of u_r in those regions.

Based on classical hydrodynamics theories, the axial, u_{ex}, and azimuthal, $u_{e\theta}$, velocities at the injector exit for an incompressible inviscid fluid can be written as follows:

$$u_{ex} = \sqrt{1 - 2(1-\varphi)^2/(2-\varphi)}, \tag{13}$$

$$u_{e\theta} = \sqrt{2(1-\varphi)^2/(2-\varphi)}, \tag{14}$$

where the coefficient of passage fullness φ is a function of the geometrical constant K,

$$K = (1-\varphi)\sqrt{2}/\varphi\sqrt{\varphi}. \tag{15}$$

Combination of Eqs. (13) and (14) gives the spreading angle of the liquid sheet at the injector exit, as defined in Eq. (4). The LOX film thickness and spreading angle are solely determined by the injector geometry and are independent of

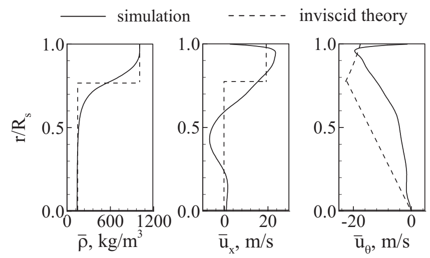

FIG. 17. Radial distributions of mean density and velocity components in the stationary region, $x/R_s=5$ (case 1: $p_\infty=10$ MPa, $T_{\mathrm{inj}}=120$ K, $T_\infty=300$ K, $\dot{m}=0.15$ kg/s, $K=3.2$, $\Delta L=2.0$ mm).

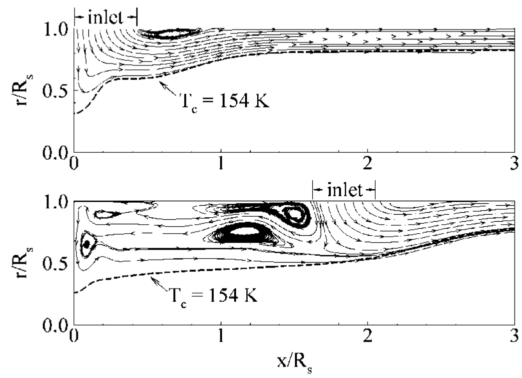

FIG. 19. Effect of tangential entry position on flow evolution near the headend ($p_\infty=10$ MPa, $T_{\mathrm{inj}}=120$ K, $T_\infty=300$ K, $\dot{m}=0.15$ kg/s, $K=3.2$).

operating conditions. The situation for a real fluid, as treated in the present study, however, may be quite different, due to the many underlying assumptions in classical theories. Figure 17 presents the radial distributions of the time-averaged density, axial velocity, and azimuthal velocity in the stationary region ($x/R_s=5$) for case 1. The discrepancies between the classical theories and the results of the present work are obvious. Nonetheless, classical hydrodynamic analysis provides much useful information about the flow physics and can serve as an effective guideline for treating injector flow dynamics.

C. Effects of flow conditions and geometry on injector behavior

The effects of LOX mass flowrate on the injector dynamics are studied in cases 1–4 (see Table II). Consistent with classical hydrodynamics theory, the calculated film thickness slightly decreases with increasing mass flowrate. The spreading angle, however, is almost independent of the variation in mass flowrate. Since both the viscous and compressibility effects are neglected, classical theory underpredicts the film thickness and overpredicts the spreading angle.

The influence of the tangential inlet position on the injector performance is explored through cases 1, 5, and 6. Figure 18 shows the corresponding axial distributions of the axial and angular momenta of the LOX film. A more severe viscous loss, as measured by the relatively smaller increase in the axial momentum, is observed for case 5 ($\Delta L=0.5$ mm) because the tangential inlet is directly attached to the headend. A similar situation occurs if the tangential inlet is placed farther downstream (case 6, $\Delta L=4.5$ mm). Under this condition, a more substantial part of the injected fluid is delivered upstream to fill the volume between the inlet and the headend and forms a recirculation region there. This is manifested by the instantaneous streamlines close to the headend for cases 5 and 6 in Fig. 19. The information obtained suggests that an optimal position for the tangential inlet exists to minimize the momentum loss. The film thickness and spreading angle at the injector exit are insensitive to the location of the tangential entry.

For injectors with large length-to-diameter (aspect) ratios, the viscous loss along the wall exerts a substantial impact on the injection process and, hence, alters the atomization efficiency and spray distribution. Figure 20 shows the relative axial- and angular-momentum losses as a function of the injector length (cases 1, 7, 8, and 9). The losses are defined as the relative drops of the momenta at the injector exit in reference to the corresponding values at the beginning of the stationary region (i.e., $x/R_s=2$). For the two shorter

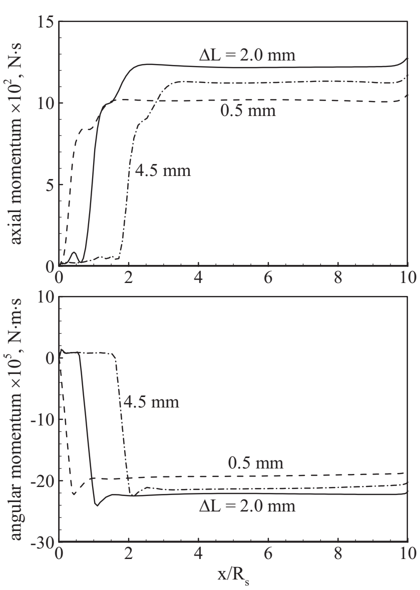

FIG. 18. Effect of tangential inlet location on mean axial- and angular-momentum distributions ($p_\infty=10$ MPa, $T_{\mathrm{inj}}=120$ K, $T_\infty=300$ K, $\dot{m}=0.15$ kg/s, $K=3.2$).

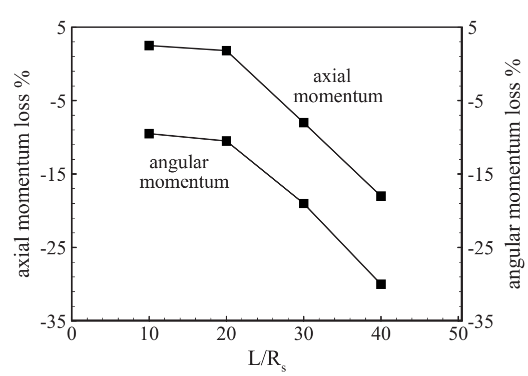

FIG. 20. Mean axial- and angular-momentum losses as functions of injector length ($p_\infty=10$ MPa, $T_{\mathrm{inj}}=120$ K, $T_\infty=300$ K, $\dot{m}=0.15$ kg/s, $K=3.2$).

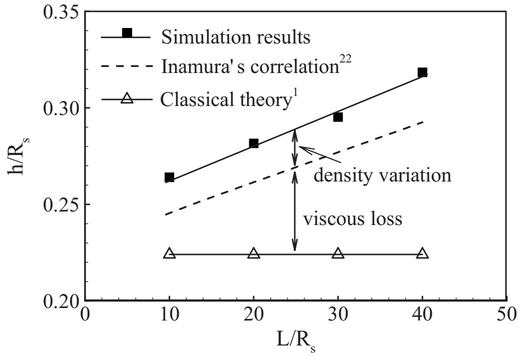

FIG. 21. LOX film thickness as function of injector length.

injectors ($L/R_s=10$ and 20), the axial momentum at the injector exit is even greater than that at the beginning of the stationary region. This phenomenon may be attributed to the transformation of the swirl-induced static pressure to the axial momentum within the acceleration regime. Since the azimuthal velocity is influenced by both the viscous dissipation and deflection of fluid in the radial direction, the angular momentum experiences a more severe decay than its axial counterpart. An increase in the injector length narrows the spreading angle. The simulation results for cases 1 and 7–9 indicate that an elongation of the injector has three negative impacts: (1) greater momentum losses, (2) thickened liquid film and enlarged mean droplet size, and (3) reduced sheet spreading angle.

Figure 21 shows the LOX film thickness at the injector exit as a function of the injector length. Classical hydrodynamics theory underestimates the film thickness by almost 30%, especially for longer injectors. An improved estimation is given by the empirical correlation suggested by Inamura *et al.*,[21] in which viscous loss is taken into account, but the influence of property variations under supercritical conditions is neglected. The latter accounts for the approximately 10% difference between the present analysis and classical theory.

Two different injector geometrical constants of $K=3.2$ and 4.2 are examined in cases 1 and 10, respectively. The mean flow properties are presented in Fig. 13. A greater geometric constant, in general, results in a stronger swirling motion, which eventually gives rise to a thinner liquid film and a wider spreading angle. Since the mixing region downstream of the injector is expanded, a better injector performance is achieved.

The effects of ambient pressure on the swirl-injector behavior are investigated for three different pressures of 100, 150, and 200 atm (i.e., cases 1, 11, and 12). As the ambient pressure increases, the momentum transfer between the LOX film and surrounding gases becomes stronger and the momentum loss, thus, increases. Consequently, the film spreading angle decreases from 73.8° for 100 atm to 71.8° for 200 atm. On the other hand, the elevated pressure tends to retard the gasification of oxygen and reduce the low-density region within the LOX film. The net result leads to a decreased film thickness with increasing pressure. The overall trend is consistent with the experimental observations of Kim *et al.*[14]

VI. SUMMARY

The flow dynamics of LOX in a pressure swirl injector with tangential entry has been investigated by means of a comprehensive numerical analysis. The formulation incorporates real-fluid thermodynamics and transport into the conservation laws to render a self-consistent approach valid for any fluid thermodynamic state.

The flow development in the injector broadly involves three different stages. LOX is introduced to the injector through the tangential inlet and occupies a bulk of the injector volume in the developing region near the headend. A thin liquid film then forms, due to centrifugal force, and convects downstream along the wall in accordance with the conservation of mass and momentum. The flow properties and film thickness vary slightly in this stationary region. Finally, the LOX flow accelerates in the axial direction as the swirl-induced pressure converts to axial momentum close to the injector exit.

Several different types of instability waves were identified to provide direct insight into the mechanisms dictating the injector flow dynamics. These include hydrodynamic instabilities in both the axial and azimuthal directions within the LOX film, acoustic waves in the gaseous core, shear-layer instabilities in the LOX sheet downstream of the injector exit, and swirling LOX-sheet induced flow recirculation near the injector exit. The interactions between those flow oscillations and their influences on the injector flow behavior were systematically examined by using the spectral and POD techniques.

A parametric study was also performed to investigate the effects of flow conditions and injector geometry on the LOX-sheet behavior. Results were compared to predictions from classical hydrodynamics theories in terms of the film thickness, spreading angle, and velocity distributions. The rapid property variations of oxygen fluid and viscous dissipation play a decisive role in determining the injector characteristics. The present work provides a quantitative basis for optimizing the injector performance.

ACKNOWLEDGMENTS

This work was sponsored by the Air Force Office of Scientific Research under Grant No. FA9550-07-1-0111 and under the STTR program through Metacomp Technologies. The authors gratefully acknowledge the support of Dr. Mitat A. Birkan, contract monitor of the program.

[1] V. G. Bazarov, V. Yang, and P. Puneesh, "Design and dynamics of jet and swirl injectors," Prog. Astronaut. Aeronaut. **200**, 19 (2004).
[2] J. Hulka and J. A. Schneider, "Single element injector cold flow testing for STME swirl coaxial injector element design," AIAA Paper No. 1993-2161, 1993.
[3] J. Hulka and J. A. Schneider, "Performance and stability of a booster class LOX/H2 swirl coaxial element injector," AIAA Paper No. 1991-1877, 1991.
[4] J. Hulka and D. Makel, "Liquid oxygen/hydrogen testing of a single swirl

coaxial injector element in a windowed combustion chamber," AIAA Paper No. 1993-1954, 1993.
[5]M. Sasaki, H. Sakamoto, M. Takahashi, T. Tomita, and H. Tamura, "Comparative study of recessed and non-recessed swirl coaxial injectors," AIAA Paper No. 1997-2907, 1997.
[6]V. G. Bazarov and V. Yang, "Liquid-propellant rocket engine injector dynamics," J. Propul. Power **14**, 797 (1998).
[7]P. G. Han, J. Seol, S. Hwang, and Y. Yoon, "The spray characteristics of swirl coaxial injectors," AIAA Paper No. 2003-0490, 2003.
[8]S. H. Kim, Y. M. Han, S. Seo, I. Y. Moon, J. K. Kim, and W. S. Seol, "Effects of LOX post recess on the combustion characteristics for Bi-swirl coaxial injector," AIAA Paper No. 2005-4445, 2005.
[9]A. H. Lefebvre, *Atomization and Sprays* (Hemisphere, New York, 1989).
[10]A. R. Jones, "Design optimization of a large pressure-jet atomizer for power plant," in *Proceeding of the Second International Conference on Liquid Atomization and Sprays, Madison, Wisconsin, 1982*.
[11]T. Marchione, C. Allouis, A. Amoresano, and F. Beretta, "Experimental investigation of a pressure swirl atomizer spray," J. Propul. Power **23**, 1096 (2007).
[12]P. A. Strakey, D. G. Talley, and J. J. Hutt, "Mixing characteristics of coaxial injectors at high gas/liquid momentum ratios," J. Propul. Power **17**, 402 (2001).
[13]D. Kim, J. H. Im, H. Koh, and Y. Yoon, "The effect of ambient gas density on the spray angle and breakup length of a swirling liquid sheet," J. Propul. Power **23**, 603 (2007).
[14]D. Kim, W. Jeong, J. Im, and Y. Yoon, "The characteristics of swirl coaxial injector under varying geometric and environmental conditions," AIAA Paper No. 2004-3521, 2004.
[15]S. K. Ela, "Subscale LOX/Hydrogen testing with a modular chamber and a swirl coaxial injector," AIAA Paper No. 1991-1874, 1991.
[16]H. Tamura, H. Sakamotot, M. Takahashi, M. Sasaki, T. Tomita, and R. Nagao, "LOX/LH2 subscale swirl coaxial injector testing," AIAA Paper No. 1997-2906, 1997.
[17]B. D. Kim and S. D. Heister, "Numerical modeling of hydrodynamic instability of swirl coaxial injector in a recessed region," AIAA Paper No. 2006-4720, 2006.
[18]B. D. Kim, S. D. Heister, and S. H. Collicott, "Three-dimensional flow simulation in the recessed region of a coaxial injector," J. Propul. Power **21**, 728 (2005).
[19]H. Park and S. D. Heister, "Nonlinear simulation of free surfaces and atomization in pressure swirl atomizers," Phys. Fluids **18**, 052103 (2006).
[20]J. V. Canino, J. Tsohas, V. Sankaran, and S. D. Heister, "Dynamic response of coaxial rocket injectors," AIAA Paper No. 2006-4707, 2006.
[21]T. Inamura, H. Tamura, and H. Sakamoto, "Characteristics of liquid film and spray injected from swirl coaxial injector," J. Propul. Power **19**, 632 (2003).
[22]V. Yang, M. Habiballah, J. Hulka, and M. Popp, editors, "Liquid rocket thrust chambers: aspects of modeling, analysis, and design," Prog. Astronaut. Aeronaut. **200** (2004).
[23]H. Meng, G. C. Hsiao, V. Yang, and J. S. Shuen, "Transport and dynamics of liquid oxygen droplets in supercritical hydrogen streams," J. Fluid Mech. **527**, 115 (2005).
[24]N. Zong, H. Meng, S. Y. Hsieh, and V. Yang, "A numerical study of cryogenic fluid injection and mixing at supercritical conditions," Phys. Fluids **16**, 4248 (2004).
[25]N. Zong and V. Yang, "Near-field flow and flame dynamics of LOX/methane shear coaxial injector under supercritical conditions," Proc. Combust. Inst. **31**, 2309 (2007).
[26]J. C. Oefelein and V. Yang, "Modeling high-pressure mixing and combustion processes in liquid rocket engines," J. Propul. Power **114**, 843 (1998).
[27]J. C. Oefelein, "Large eddy simulation of turbulent combustion processes in propulsion and power systems," Prog. Aerosp. Sci. **42**, 2 (2006).
[28]G. Erlebacher, M. Y. Hussaini, C. G. Speziale, and T. A. Zang, "Toward the large eddy simulation of compressible turbulent flows," J. Fluid Mech. **238**, 155 (1992).
[29]U. Piomelli, P. Moin, and J. H. Ferziger, "Model consistency in the large eddy simulation of turbulent channel flows," Phys. Fluids **31**, 1884 (1988).
[30]M. S. Graboski and T. E. Daubert, "A modified Soave equation of state for phase equilibrium calculation. 1. Hydrocarbon systems," Ind. Eng. Chem. Process Des. Dev. **17**, 443 (1978).
[31]V. Yang, "Modeling of supercritical vaporization, mixing, and combustion processes in liquid-fueled propulsion systems," Proc. Combust. Inst. **28**, 925 (2000).
[32]J. F. Ely and H. J. Hanley, "Prediction of transport properties. 1. Viscosity of fluids and mixtures," Ind. Eng. Chem. Fundam. **20**, 323 (1981).
[33]J. F. Ely and H. J. Hanley, "Prediction of transport properties. 2. thermal conductivity of pure fluids and mixtures," Ind. Eng. Chem. Fundam. **22**, 90 (1983).
[34]S. Takahashi, "Preparation of a generalized chart for diffusion coefficients of gases at high pressures," J. Chem. Eng. Jpn. **7**, 417 (1974).
[35]H. Meng and V. Yang, "A unified thermodynamics treatment of general fluid mixtures and its application to a preconditioning scheme," J. Comput. Phys. **189**, 277 (2003).
[36]N. Zong, "Modeling and simulation of cryogenic fluid injection and mixing dynamics under supercritical conditions," Ph.D. thesis, Pennsylvania State University, 2005.
[37]S. Y. Hsieh and V. Yang, "A preconditioned flux-differencing scheme for chemically reacting flows at all Mach numbers," Int. J. Comput. Fluid Dyn. **8**, 31 (1997).
[38]M. M. Rai and S. Chakravarthy, "Conservative high-order-accurate finite-difference methods," AIAA Paper No. 1993-3380, 1993.
[39]G. Comte-Bellot and S. Corrsin, "Simple Eulerian time correlation of full- and narrow-band velocity signals in grid-generated, isotropic turbulence," J. Fluid Mech. **48**, 273 (1971).
[40]R. C. Swanson and E. Turkel, "On central difference and upwind schemes," J. Comput. Phys. **101**, 292 (1992).
[41]V. R. Rubinsky, "Combustion instability in the RD-0110 engine," Prog. Astronaut. Aeronaut. **169**, 89 (1996).
[42]N. Zong and V. Yang, "Cryogenic fluid jets and mixing layers in transcritical and supercritical environment," Combust. Sci. Technol. **178**, 193 (2006).
[43]T. Poinsot and S. Lele, "Boundary conditions for direct simulation of compressible viscous flows," J. Comput. Phys. **101**, 104 (1992).
[44]P. K. Kundu and I. M. Cohen, *Fluid Mechanics*, 2nd ed. (Academic, San Diego, 2001).
[45]S. Wang and V. Yang, "Unsteady flow evolution in swirl injectors, Part II: External excitations," Phys. Fluids **17**, 045107 (2005).
[46]V. Yang and W. E. Anderson, editors, "Liquid rocket engine combustion instability," Prog. Astronaut. Aeronaut. **169** (1996).
[47]Y. Huang, S. Wang, and V. Yang, "A systematic analysis of combustion dynamics in a lean-premixed swirl-stabilized combustor," AIAA J. **44**, 724 (2006).
[48]K. C. Schadow and E. Gutmark, "Combustion instability related to vortex shedding in dump combustors and their passive control," Prog. Energy Combust. Sci. **18**, 117 (1992).
[49]C. W. Rowley, T. Colonius, and R. M. Murray, "Model reduction for compressible flows using pod and Galerkin projection," Physica D **189**, 115 (2004).
[50]G. Berkooz, P. Holmes, and J. L. Lumley, "The proper orthogonal decomposition in the analysis of turbulent flows," Annu. Rev. Fluid Mech. **25**, 539 (1993).
[51]J. Panda and D. K. McLanghlin, "Experiments on the instabilities of a swirling jet," Phys. Fluids **6**, 263 (1994).